optica

Photoacoustic Brillouin spectroscopy of gas-filled anti-resonant hollow-core optical fibers

Yan Zhao,[1,2] Yun Qi,[1,2] Hoi Lut Ho,[1,2] Shoufei Gao,[1] Yingying Wang,[3] and Wei Jin[1,2,*]

[1]Department of Electrical Engineering, The Hong Kong Polytechnic University, Hong Kong SAR, China
[2]Photonics Research Center, The Hong Kong Polytechnic University Shenzhen Research Institute, Shenzhen, China
[3]Institute of Photonics Technology, Jinan University, Guangzhou, China
*Corresponding author: wei.jin@polyu.edu.hk

Received 14 December 2020; revised 14 March 2021; accepted 18 March 2021 (Doc. ID 417235); published 12 April 2021

Photoacoustic spectroscopy, a powerful tool for gas analysis, typically uses bulky gas cells and discrete microphones. Here we exploit light-gas-acoustic interaction in a gas-filled anti-resonant hollow-core-fiber (AR-HCF) to demonstrate photoacoustic Brillouin spectroscopy (PABS). Pump absorption of gas molecules excites the acoustic resonances of the fiber, which modulates the phase of a probe beam propagating in the fiber. Detection of the phase modulation enables spectroscopic characterization of gas species and concentration as well as the fiber microstructure. Studying the acoustic resonances allows us to characterize the longitudinal inhomogeneity of the fiber microstructure. By tuning the pump modulation frequency to a wine-glass-like capillary mode of a 30-cm-long AR-HCF and the pump wavelength across a gas absorption line, we demonstrate detection of acetylene at the parts-per-billion level. PABS has great potential for high sensitivity gas sensing and non-invasive fiber characterization.

https://doi.org/10.1364/OPTICA.417235

1. INTRODUCTION

Photoacoustic spectroscopy (PAS) is a powerful tool for tracing gas by detecting the acoustic wave generated during optical absorption [1,2]. Typically, an open-path absorption cell is used for photoacoustic generation, and a microphone is used for acoustic detection. The types of microphones used include a quartz tuning fork [3], interferometric cantilever [4], fiber-optic microphone [5], etc. The detection sensitivity can be enhanced by using an additional resonant acoustic cavity [6], and a parts-per-billion (ppb) level or lower limit of detection has been demonstrated for a variety of gases [7–11].

Forward Brillouin scattering (FBS) refers to the process of acousto-optic interaction between an optical mode and a guided acoustic mode in a waveguide. The acoustic wave is excited by optical forces such as electrostriction and radiation pressure, and the resonant accumulation of acoustic energy occurs when the acoustic frequency matches to an acoustic mode of the waveguide, enabling enhanced photon–phonon interaction along the waveguide. FBS has been demonstrated on a variety of platforms, including single-mode fibers (SMFs) [12], multi-core fibers [13], solid-core photonic crystal fibers [14–16], and integrated silicon waveguides [17], and has been exploited for sensing [18–21], coherent information processing [22], optical amplification [23] and lasing [24], frequency comb generation [16], mode-locked lasers [25], etc. Recently, Brillouin scattering in hollow-core fibers (HCFs) has been studied [26–31]. Intense backward stimulated Brillouin scattering was observed at high gas pressures and was used for lasing and distributed temperature sensing [30]. However, FBS at atmospheric pressure is extremely weak in HCFs, and no useful application has been reported to the best of our knowledge.

Here, we demonstrate that the acoustic mode can be excited by optical absorption of gas molecules inside an anti-resonant HCF (AR-HCF) via the photoacoustic effect, and the excitation can be two orders of magnitude more efficient than by the optical forces. We then report a new approach of PAS by exploiting the enhanced interaction of the acoustic mode with a probe optical mode in the AR-HCF, which is named photoacoustic Brillouin spectroscopy (PABS). The AR-HCF, as a vibroacoustic system, offers a gas-filled region for acoustic wave generation and silica microstructures as an acoustic resonator. The acoustic wave generated by optical absorption is resonantly amplified in the fiber and modulates the phase of a probe light beam propagating along the fiber. The accumulated phase modulation is measured by a dual-mode interferometer formed in the same AR-HCF, which has the advantages of simplicity in system setup and stability against environment disturbance [32]. The acoustic resonances detected by PABS reveal the delicate microstructures of the AR-HCF and can be used to characterize the inhomogeneity along the fiber. The optical spectral absorption at an acoustic resonance provides a means of photoacoustic gas spectroscopy with enhanced sensitivity.

2. PRINCIPLE OF PABS IN AR-HCF

A. Acoustic Mode in AR-HCF

Figure 1(a) shows a scanning electron microscopy (SEM) image of the AR-HCF used in the experiment. It consists of an air-core and

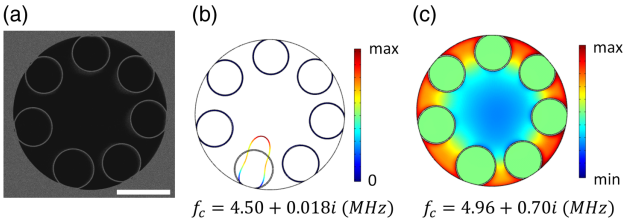

Fig. 1. (a) SEM image of the AR-HCF. The white bar is 20 μm. Capillaries have slightly different sizes. (b) A capillary mode (w_1). The deformation of the capillary is enlarged for clarity. (c) An air mode (R_{01}). The geometry of the AR-HCF used for simulation is built from the SEM image of the real AR-HCF, and the simulation is conducted at 293.15 K and 1 bar (see Supplement 1 for details).

seven suspended silica capillaries of slightly different sizes. Finite-element-method (FEM) analysis based on the thermo-viscous acoustic model shows that the fiber supports a few coupled acoustic modes in the frequency range up to 8 MHz.

Intuitively, the structure of a gas-filled AR-HCF supports acoustic modes in air (termed air mode) and silica capillaries (termed capillary modes [29]). They form hybrid acoustic modes. The air mode is described by the density change (ρ), which accounts for both pressure change and temperature change. The capillary mode is described by the displacement of the silica capillary (w).

As examples, Fig. 1(b) shows a capillary mode (the first-order wine-glass-like mode w_1) with an eigenfrequency of $4.50 + 0.018i$ MHz. The imaginary part of the eigenfrequency accounts for the loss of the mode. The loss of the capillary mode is dominantly due to air damping. Figure 1(c) shows an air mode (the first-order radial-like mode R_{01}) with an eigenfrequency of $5.15 + 0.70i$ MHz, which is more lossy compared with the capillary mode. There are seven similar capillary modes, corresponding to the number of capillaries. The different sizes of capillaries reduce their coupling to the air mode and also reduce the loss of capillary modes. With increasing gas pressure, the loss of air mode reduces, while the loss of capillary mode increases due to stronger air damping. Hence, the capillary mode would dominate at atmospheric and lower pressures, while the air mode would dominate at high pressures.

Different from the commonly used methods to excite FBS, here, an acoustic mode is excited via the photoacoustic effect by gas absorption of a modulated pump laser beam propagating in the gas-filled AR-HCF. The wavelength (λ_P) of the pump is tuned to an absorption line of the gas and the modulation frequency (f) of pump to the frequency of an acoustic mode. At low frequency of several megahertz (MHz), the acoustic mode is very close to cutoff and almost transverse, and the eigenfrequency may be approximated by the cutoff frequency f_c. Hence, the FBS is also referred to as Raman-like scattering [14].

Considering a simplified two-level system, the amplitude of the acoustic signal is proportional to the optical absorption induced harmonic heat source $Q \propto \alpha C P_P / \sqrt{\Omega^2 \tau^2 + 1}$, where α is the absorption coefficient, C is the gas concentration, P_P is the pump power, $\Omega = 2\pi f$, and τ is the thermal relaxation time of the system. For many gases or gas mixtures, the values of τ are in the range of micro- to nanoseconds [33,34], and, hence, the photoacoustic effect is particularly suited for exciting the lowest-order capillary and air acoustic modes of the AR-HCF, which is in the frequency range of MHz.

B. Probe the Acoustic Modes with an Optical Wave

The acoustic resonances or modes may be detected by co-propagating a probe beam (λ_L) with the pump beam (λ_P) in the gas-filled AR-HCF. Acousto-optic interaction over the length of the fiber modulates the phase of the probe, which can be detected by optical interferometry. The AR-HCF used here primarily supports two groups of optical modes (i.e., LP_{01} and LP_{11}), and, due to different overlap with the acoustic modes, the phases of the two optical modes are modulated differently by the acoustic resonances. We choose to use a mode interference method to measure the phase difference between the two optical modes. The index difference between LP_{01} and LP_{11} modes, $\Delta n = n_{01} - n_{11}$, depends on the size of the hollow core and is in general smaller for a larger-core diameter [35]. For the fiber shown in Fig. 1(a), the index difference is about 10^{-3}. The differential phase is insensitive to external disturbance due to common-path noise cancellation. Compared with the phase modulation of an individual mode, the differential phase is more robust against environment disturbance with an enhanced noise rejection ratio on the order of $n_{01}/\Delta n$ [32].

The phase modulation exerted on a probe optical mode results mainly from two contributing factors, the gas density change [36] and the shifting boundary of silica capillaries [37]. It includes two parts: a non-resonant part due to the temperature modulation of gas induced by optical absorption, named photothermal phase modulation; a resonant part due to the photoacoustically excited acoustic resonance. The differential phase modulation may be calculated by using $\Delta\phi = (2\pi/\lambda_L) \int_0^L dz[\Delta n_{01}(z) - \Delta n_{11}(z)]$ and expressed in the form of

$$\Delta\phi(\Omega, \lambda_P) = \xi(\Omega)\alpha(\lambda_P) C L_{\text{eff}} P_P, \tag{1}$$

where $L_{\text{eff}} = (1 - e^{-\alpha CL})/\alpha C$ is the effective interaction length of the AR-HCF, and it approximates the length of fiber when $\alpha CL \ll 1$, assuming the loss of AR-HCF can be ignored. ξ is a normalized phase modulation coefficient that describes the frequency response of the fiber and would become significant around the acoustic resonances. We could define a photoacoustic Brillouin nonlinear coefficient $\gamma = \xi(\Omega)\alpha(\lambda_P)C$. Since $\Delta\phi(\Omega, \lambda_P)$ is a function of the modulation frequency $\Omega = 2\pi f$ and the wavelength of pump λ_P, the proposed PABS method may be used for gas spectroscopy via the $\alpha(\lambda_P)C$ dependence and for spectroscopy of microstructure via the $\xi(\Omega)$ dependence.

3. RESULT

A. Experiment Setup

The experiment setup is shown in Fig. 2(a). The pump laser is a distributed feedback (DFB) laser with a wavelength at 1532.83 nm, which is near the P(13) absorption line of acetylene. The wavelength of the pump is tuned across the absorption line by thermal tuning, and the intensity of the pump is modulated sinusoidally at the frequency of Ω by use of an acoustic optical modulator (AOM). The pump power is further amplified by an erbium-doped fiber amplifier (EDFA). An optical bandpass filter (BPF) is used to filter out the amplified spontaneous emission noise from the EDFA. The 3 dB bandwidth of the BPF is about 1 nm. The probe light is from an external cavity diode laser (ECDL) and is

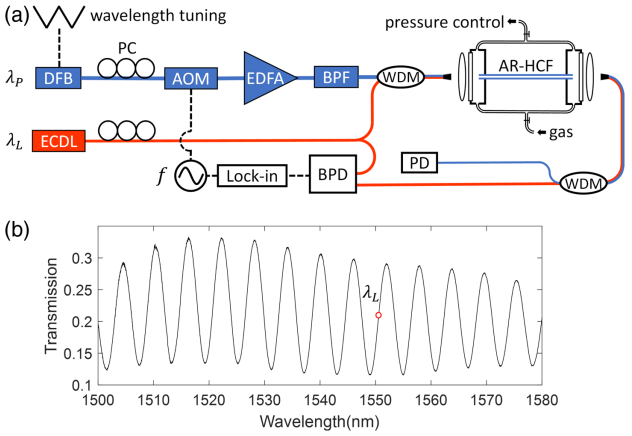

Fig. 2. (a) Experiment setup for PABS in an AR-HCF. Light is coupled into AR-HCF with optical fiber collimators and optical lenses. λ_P and λ_L, wavelengths of pump and probe laser beams; PC, polarization controller; ECDL, external cavity diode laser; PD, photodetector; BPD, balanced photodetector. (b) Transmission spectrum of the AR-HCF dual-mode interferometer. The red circle indicates the wavelength of the probe at a quadrature point of the interferogram.

multiplexed/de-multiplexed with the pump beam by wavelength-division multiplexers (WDMs). Optical lenses are used to couple light into and collect light from the AR-HCF.

By using lateral offset coupling, both LP_{01} and LP_{11} modes are excited in the AR-HCF and combined at the output SMF to form a dual-mode optical interferometer for the probe beam. The polarization controller (PC) and optical lenses are carefully adjusted to achieve maximum fringe contrast at the interferometer output. Figure 2(b) shows the transmission spectrum of the modal interferometer measured with a broadband light source and an optical spectrum analyzer. The near perfect sinusoidal interference spectrum indicates that only two spatial optical modes (i.e., LP_{01} and LP_{11}) are guided in the AR-HCF. The probe laser wavelength λ_L is then fixed at the quadrature point of an interference fringe. The probe beam is detected by a balanced photodetector to reduce the effect of intensity noise. A lock-in amplifier is used to measure the harmonic signal at the modulation frequency $f = \Omega/2\pi$.

B. PABS of Fiber Microstructure

We first measured the PABS signal of a 30-cm-long AR-HCF (fiber sample A) filled with pure C_2H_2 at a pressure of 10 mbar. The gas filling time can be down to 20 s by pressurizing gas into the fiber. Figure 3(a) shows the measured probe phase modulation in the frequency range from 25 kHz to 7 MHz when the pump is tuned to the P(13) absorption line of the $\nu_1 + \nu_3$ band of acetylene (blue trace). Seven strong resonances are observed around 5 MHz, corresponding to the seven capillaries of the AR-HCF. The Fano-like profiles are possibly due to the photothermal phase modulation not

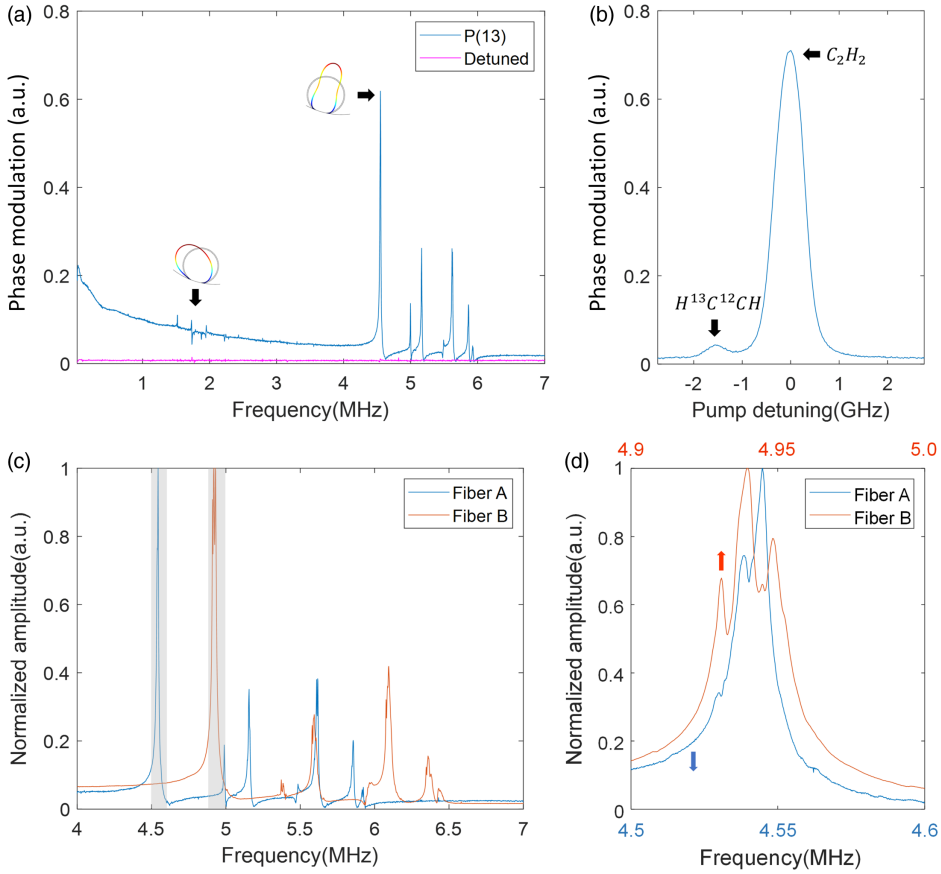

Fig. 3. PABS spectra of 30-cm-long AR-HCFs filled with 10 mbar pure C_2H_2. (a) The frequency response of fiber A. The blue and red curves are measured by tuning the pump to the P(13) absorption line and away from P(13) to 1532.7 nm, respectively. (b) The absorption spectrum of C_2H_2 measured with PABS with fiber A with pump modulation frequency fixed at 4.545 MHz. (c) Comparison of the frequency response of two 30-cm-long AR-HCF samples (fibers A and B). (d) A closer look of the gray regions in (c) with their frequencies shown on the bottom (blue) for fiber A and on the top (red) for fiber B, respectively.

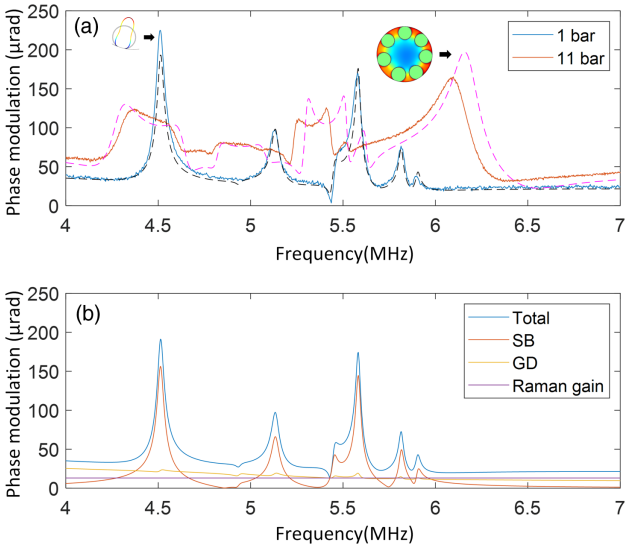

Fig. 4. (a) Frequency dependence of probe phase modulation for fiber A at the pressures of 1 bar and 11 bar. The phase modulation is retrieved from the interferogram of the modal interferometer (see Supplement 1 for details). The dashed line shows the simulation results. The simulation is based on a model built from the SEM of the sample. (b) Contribution of phase modulation due to shifting boundary (SB), gas density change (GD), and the Raman gain of SMF pigtails (see Supplement 1 for details).

being in phase with the acoustic resonances. The capillary modes are stimulated by optical absorption. When the pump wavelength is tuned away from the absorption line, the phase modulation reduces to nearly zero (red trace). The small background signal is believed to be stimulated by the electrostriction and radiation pressure of the pump beam, which is about 200 times weaker than the largest PABS resonance. We also measured the gas absorption spectrum with pump modulation frequency fixed at an acoustic resonance while sweeping the pump wavelength across the P(13) absorption line of acetylene around 1532.83 nm. A Doppler limited lineshape is observed, and an isotope of C_2H_2 is resolvable, as shown in Fig. 3(b).

For comparison, we conducted the experiment with another piece of 30-cm-long AR-HCF (labeled as fiber sample B) from the same fiber drawing process. As shown in Fig. 3(c), the two samples show similar acoustic responses, but the response for fiber B is upshifted by about 8%. The upshift is due to the scaling of the fiber structure during the drawing process. The blow-up of one of the capillary modes near 4.55 MHz and 4.95 MHz is shown in Fig. 3(d). The measured Q-factors of the capillary mode of fibers A and B are, respectively, about 480 and 256, which is smaller than the calculated Q-factor limited by gas damping of C_2H_2 (about 940). The multi-peak spectra are due to the inhomogeneity of the capillary along the fiber over a length of $L_{\text{eff}} = 76$ mm, the effective absorption distance for pure acetylene at 10 mbar. For fiber A, the frequency difference between the two peaks is about $\Delta f = 6$ kHz. FEM analysis shows that such a frequency difference is equivalent to a wall thickness variation of 0.5 nm or a capillary diameter variation of 28 nm, corresponding to an inhomogeneity of 1.6%/m in the wall thickness or 2.4%/m in the capillary diameter. This value is quite close to the inhomogeneity estimated by the relative change of the resonant frequency $\Delta f/(f_c L_{\text{eff}}) = 1.7\%/\text{m}$. For fiber B, the inhomogeneity is estimated to be 2.3%/m in the wall thickness or 3.6%/m in the capillary diameter.

We conducted further experiments with fiber A for gas pressure from 1 to 11 bar. The fiber is now filled with 106 ppm C_2H_2 balanced with nitrogen. Pump depletion may be ignored in this experiment because of the low concentration of C_2H_2. The experimental results are shown in Fig. 4(a). At a pressure of 11 bar, the air mode dominates, and the first-order radial-like mode is observed. The frequency shift of the capillary modes is due to the coupling with the air mode. The coupling between the capillary mode and the air mode gives them a complicated dependence on the gas pressure. We numerically calculate the phase modulation, and the result matches well with our experiment. As shown in Fig. 4(b), at a pressure of 1 bar, the signal detected consists of the phase modulation induced by the shifting boundary, the gas density change, and the Raman gain of SMF pigtails. For air mode dominated situations, for example, the radial air mode (R_{01} etc.), they are proportional to the gas pressure. The small compressibility of gas at high pressure reduces the acoustic attenuation in gas, which results in a higher amplitude of the air mode. However, the irregular silica-air boundary of AR-HCF introduces additional viscous and thermal dissipation at the boundary.

C. PABS for Gas Sensing

Gas detection with PABS was performed with fiber A by employing the capillary acoustic mode at 4.51 MHz, which gives a Q-factor

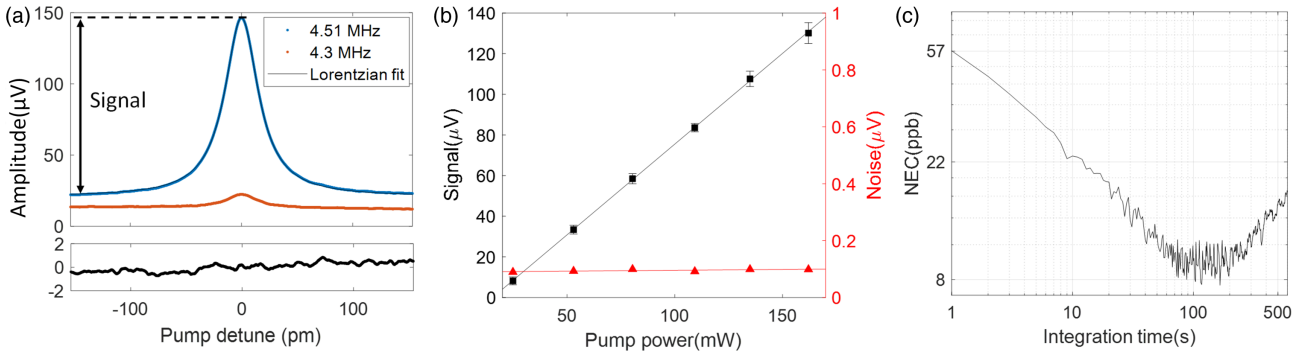

Fig. 5. (a) Results of gas detection experiment with fiber A filled with 106 ppm C_2H_2 balanced with nitrogen at a pressure of 1 bar. The time constant of the lock-in amplifier is 1 s with a filter slope of 18 dB/Oct. (a) The measured PABS signal around the P(13) absorption line of C_2H_2. The blue and red curves show the spectrum at resonance and off-resonance, respectively. The blue curve can be well fitted to a Lorentzian lineshape, and the residuals are shown as the black curve. The residuals are mainly due to the power drift during the tuning of the pump. (b) The power dependence of the photoacoustic signal. The error bar for the signal is enlarged 20 times for clarity. (c) Allan deviation analysis of noise by offsetting the wavelength of the pump to 1532.7 nm.

about 120 at the pressure of 1 bar. The differential phase modulation of the capillary mode at 1 bar is about 20% larger than that of the strongest air mode (the second-order radial mode) at 11 bar. We measure the absorption spectrum of C_2H_2 by fixing the pump modulation frequency to 4.51 MHz and slowly sweeping the wavelength of the pump laser across the P(13) absorption line near 1532.83 nm. The acoustic signal is defined as the amplitude subtracted by the background, as shown in Fig. 5(a). The background is due the Raman gain of SMF pigtails (see Supplement 1 for details). As shown in Fig. 5(a), the acoustic signal is enhanced by about 14 times when compared with the non-resonant signal at 4.3 MHz. The absorption spectrum has a Lorentzian lineshape.

The measured photoacoustic signal is proportional to the pump power, as shown in Fig. 5(b). The maximum amplitude is about 122 μV. The maximum phase modulation is estimated to be 214 μrad with a 162 mW pump power and 106 ppm C_2H_2, corresponding to a normalized phase modulation coefficient of $\xi_{max} = 0.39$ rad/W or a photoacoustic Brillouin nonlinear coefficient of $\gamma_{max} = 4.4 \times 10^{-3}\ \mathrm{W^{-1}m^{-1}}$ for 106 ppm C_2H_2. The Brillouin nonlinear coefficient could be further increased by using a higher concentration of C_2H_2. Allan analysis is performed based on the measurement data obtained over a period of 3600 s when the pump was tuned away from the absorption line to 1532.7 nm, and the results are shown in Fig. 5(c). The noise level is about 9.1 nV for an integration time of 100 s, giving a signal-noise-ratio of 13,406. The noise-equivalent concentration is calculated to be 8 ppb.

4. DISCUSSION AND CONCLUSIONS

In conclusion, we demonstrated PABS of gas-filled HCFs. Study of the intriguing acoustic resonances of the AR-HCFs reveals its delicate microstructures and allows characterization of inhomogeneity along the fiber. Experiments with fiber samples from the same fiber drawing process reveal longitudinal inhomogeneity of a few percent per meter along the fiber. By employing a wine-glass-like acoustic mode of the silica capillary, we demonstrate a PABS for gas sensing with a noise-equivalent concentration of 8 ppb C_2H_2.

Compared with FBS in AR-HCF stimulated by electrostriction and radiation pressure, the strength of PABS is about 200 times larger even with a relatively low concentration (i.e., 106 ppm) of C_2H_2, which makes it possible for fiber characterization and sensing applications. Besides, HCFs may be filled with different gas species and different concentrations to provide flexibility to engineer the acoustic property of the fiber.

The approach of PABS demonstrated here is very different from the traditional methods of PAS. It has unique advantages. First, compared with traditional methods, our approach allows the accumulation of acoustic signals simultaneously in an acoustic mode and along the fiber length. The total acoustic signal is proportional to the Q-factor of the acoustic mode as well as the length of the HCF. Second, the detection of differential phase modulation reduces the noise level of PAS and makes it more robust against environmental perturbations. In addition, using a light beam propagating in the same HCF as the acoustic probe avoids the use of an additional microphone, which intrinsically minimizes the disturbance of the microphone on the acoustic mode. HCFs may be conveniently integrated into standard fiber-based systems for cost-effective sensors and instruments with compact size and remote detection capability.

Different probe optical modes have different phase sensitivities to the acoustic mode. For the AR-HCF we used, the phases of the high-order optical modes are more sensitive to the capillary mode, since the optical field intensities are stronger in the vicinity of the silica-gas boundary. The maximum displacement of the capillary mode w_1 is about $\delta = 2.9$ pm, corresponding to a sensitivity to the deflection of about $|\partial n_{11b}/\partial\delta| \approx 41\ \mathrm{m^{-1}}$ for the most sensitive LP_{11b} mode. From another perspective, increasing the sensitivity of the probe on the acoustic mode is actually equivalent to maximizing the work done by its optical force during an acoustic period. The sensitivity can be enhanced by optimizing the waveguide structure. For example, the parallel evanescent-field-bonding

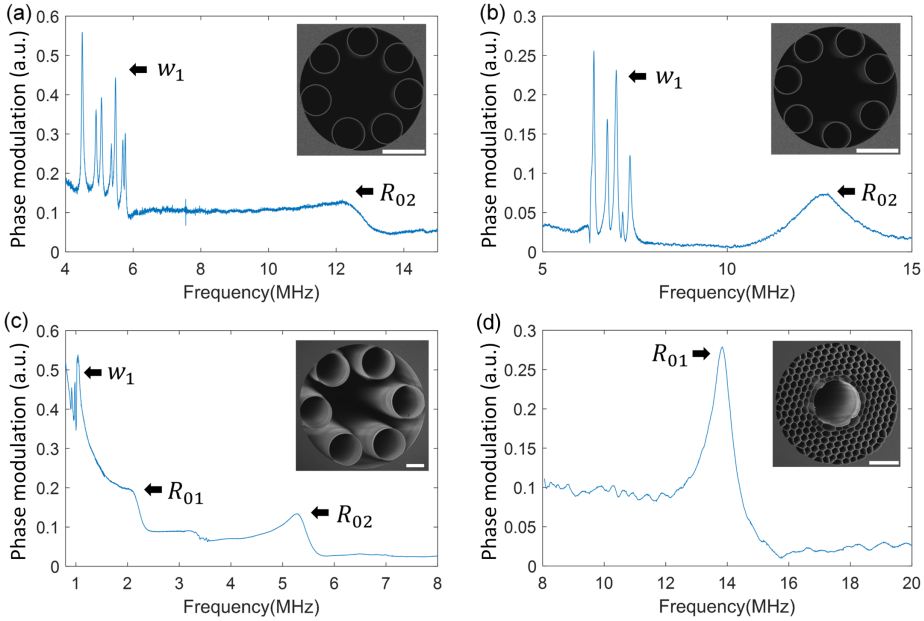

Fig. 6. PABS of different HCFs at a pressure of 1 bar. The inset shows the SEM image of the HCF. The white bar is 20 μm. The result is measured with a pump power of 162 mW, and the 30-cm-long HCFs are filled with 106 ppm C_2H_2. PABS signal of the PBG-HCF [Fig. 5(d)] is measured with a Mach–Zehnder interferometer with the PBG-HCF as one of the arms.

waveguides [38–40] could increase the sensitivity on the acoustic mode significantly. A sensitivity of $|\partial n_{\text{eff}}/\partial\delta| = 64 \times 10^3\ \text{m}^{-1}$ has been demonstrated on a dual-nanoweb fiber [40]. In our experiment, the AR-HCF is not designed for high-Q acoustic performance. A well-designed wine-glass mode of a silica capillary could reach a Q-factor of a few thousands under atmospheric condition [41] and could be even higher at lower pressures. The length of AR-HCF can also be at least 100 times longer, providing that the inhomogeneity is not a problem. For a longer HCF, microchannels may be fabricated along the fiber to speed up the gas filling process [42]. A potential enhancement of the PABS signal by several orders of magnitude is possible under atmospheric conditions.

Compared with photothermal spectroscopy with HCFs [32,43], PABS measures the acoustic resonances instead of the gas temperature change in the fibers. HCFs, which are typically made of silica, are not good at confining heat. The heat generated due to optical absorption is easily dissipated into the environment via the silica cladding. However, the microstructure of the fibers can resonantly accumulate acoustic waves with a Q-factor of a few hundred. As shown in Fig. 3(a), the photoacoustic signal at 4.51 MHz is much higher and even higher than the photothermal signal at a few kilohertz, which allows the system to work at a higher frequency to minimize the '$1/f$' noise. Furthermore, the probe optical mode could be made much more sensitive to the acoustic mode by optimizing the fiber microstructure, as discussed above. We believe that PABS would represent a new paradigm for highly sensitive gas detection by further exploiting the opto-acoustic interaction in micro-structured fibers.

The highly tailorable microstructure of HCFs gives them intriguing acoustic properties. It has been a challenge to characterize the delicate microstructure of HCFs non-invasively. Recently, measurement of the capillary sizes of AR-HCFs by using whispering gallery mode spectroscopy has been reported [44]. PABS of HCFs provides an alternative method to characterize the microstructures. We have performed PABS of several different HCFs, and the results are shown in Fig. 6. For the AR-HCFs in Figs. 6(a)–6(c), both the capillary mode (w_1) and the air mode (R_{01} and R_{02}) are observed. For the photonic bandgap (PBG) HCF in Fig. 6(d), the R_{01} air mode is clearly visible, and the ripples around the air mode would be due to the seriously damped acoustic resonances of the complex cladding microstructure. The capillary mode of AR-HCF could be used to characterize the relative sizes as well as the longitudinal inhomogeneity of the capillaries.

The ultimate Q-factor of the capillary mode of HCFs might be limited by the surface roughness from the frozen surface capillary wave during the fiber fabrication [45]. In our experiment, the estimated maximum displacement of the capillary is about a few picometers, which is much smaller than the rms surface roughness (about 0.1 nm [46]). By using a short length of AR-HCF or AR-HCF with very good inhomogeneity, it might be possible to characterize the surface roughness of HCFs, which accounts for an important optical loss mechanism of them. Furthermore, the concept of PABS demonstrated here is not limited to HCFs. It could be applied on other platforms such as opto-mechano-fluidic resonators [47], dual-nanoweb fibers [40], and integrated photonic circuits [39].

Funding. National Key Research and Development Program of China (2019YFB2203904); Hong Kong SAR government GRF grant (15212220); National Natural Science Foundation of China (61827820); Local Innovative and Research Teams Project of Guangdong Pear River Talents Program (2019BT02X105); Hong Kong Polytechnic University (1-9B65, YW4C).

Acknowledgment. The authors acknowlege Prof. Lixi Huang at The University of Hong Kong for helpful discussions and suggestions. The photonic bandgap hollow-core fiber was kindly provided by Michael Frosz at the Max Planck Institute for the Science of Light in Erlangen, Germany.

Disclosures. The authors declare no conflicts of interest.

Data Availability. Data underlying the results presented in this paper are not publicly available at this time but may be obtained from the authors upon reasonable request.

Supplemental documents. See Supplement 1 for supporting content.

REFERENCES

1. G. A. West, J. J. Barrett, D. R. Siebert, and K. V. Reddy, "Photoacoustic spectroscopy," Rev. Sci. Instrum. **54**, 797–817 (1983).
2. F. J. Harren and S. M. Cristescu, "Photoacoustic spectroscopy in trace gas monitoring," in *Encyclopedia of Analytical Chemistry: Applications, Theory and Instrumentation* (2006), pp. 1–29.
3. A. A. Kosterev, Y. A. Bakhirkin, R. F. Curl, and F. K. Tittel, "Quartz-enhanced photoacoustic spectroscopy," Opt. Lett. **27**, 1902–1904 (2002).
4. V. Koskinen, J. Fonsen, K. Roth, and J. Kauppinen, "Progress in cantilever enhanced photoacoustic spectroscopy," Vib. Spectrosc. **48**, 16–21 (2008).
5. Y. Tan, C. Zhang, W. Jin, F. Yang, H. L. Ho, and J. Ma, "Optical fiber photoacoustic gas sensor with graphene nano-mechanical resonator as the acoustic detector," IEEE J. Sel. Top. Quantum Electron. **23**, 199–209 (2016).
6. A. Miklós, P. Hess, and Z. Bozóki, "Application of acoustic resonators in photoacoustic trace gas analysis and metrology," Rev. Sci. Instrum. **72**, 1937–1955 (2001).
7. S. Bernegger and M. Sigrist, "CO-laser photoacoustic spectroscopy of gases and vapours for trace gas analysis," Infrared Phys. **30**, 375–429 (1990).
8. S. T. L. Hekkert, M. J. Staal, R. H. M. Nabben, H. Zuckermann, S. Persijn, L. J. Stal, L. A. Voesenek, F. J. M. Harren, J. Reuss, and D. H. Parker, "Laser photoacoustic trace gas detection, an extremely sensitive technique applied in biological research," Instrum. Sci. Technol. **26**, 157–175 (1998).
9. L. Dong, A. A. Kosterev, D. Thomazy, and F. K. Tittel, "QEPAS spectrophones: design, optimization, and performance," Appl. Phys. B **100**, 627–635 (2010).
10. V. Spagnolo, P. Patimisco, S. Borri, G. Scamarcio, B. E. Bernacki, and J. Kriesel, "Part-per-trillion level SF_6 detection using a quartz enhanced photoacoustic spectroscopy-based sensor with single-mode fiber-coupled quantum cascade laser excitation," Opt. Lett. **37**, 4461–4463 (2012).
11. T. Tomberg, M. Vainio, T. Hieta, and L. Halonen, "Sub-parts-per-trillion level sensitivity in trace gas detection by cantilever-enhanced photo-acoustic spectroscopy," Sci. Rep. **8**, 1848 (2018).
12. R. Shelby, M. Levenson, and P. Bayer, "Guided acoustic-wave Brillouin scattering," Phys. Rev. B **31**, 5244–5252 (1985).
13. H. H. Diamandi, Y. London, and A. Zadok, "Opto-mechanical inter-core cross-talk in multi-core fibers," Optica **4**, 289–297 (2017).
14. P. Dainese, P. St.J. Russell, G. S. Wiederhecker, N. Joly, H. L. Fragnito, V. Laude, and A. Khelif, "Raman-like light scattering from acoustic phonons in photonic crystal fiber," Opt. Express **14**, 4141–4150 (2006).
15. P. Dainese, P. St.J. Russell, N. Joly, J. Knight, G. S. Wiederhecker, H. L. Fragnito, V. Laude, and A. Khelif, "Stimulated Brillouin scattering from multi-GHz-guided acoustic phonons in nanostructured photonic crystal fibres," Nat. Phys. **2**, 388–392 (2006).
16. M. S. Kang, A. Nazarkin, A. Brenn, and P. St.J. Russell, "Tightly trapped acoustic phonons in photonic crystal fibres as highly nonlinear artificial Raman oscillators," Nat. Phys. **5**, 276–280 (2009).
17. H. Shin, W. Qiu, R. Jarecki, J. A. Cox, R. H. Olsson, A. Starbuck, Z. Wang, and P. T. Rakich, "Tailorable stimulated Brillouin scattering in nanoscale silicon waveguides," Nat. Commun. **4**, 1944 (2013).
18. Y. Antman, A. Clain, Y. London, and A. Zadok, "Optomechanical sensing of liquids outside standard fibers using forward stimulated Brillouin scattering," Optica **3**, 510–516 (2016).

19. D. M. Chow, Z. Yang, M. A. Soto, and L. Thévenaz, "Distributed forward Brillouin sensor based on local light phase recovery," Nat. Commun. **9**, 2990 (2018).
20. G. Bashan, H. H. Diamandi, Y. London, E. Preter, and A. Zadok, "Optomechanical time-domain reflectometry," Nat. Commun. **9**, 2991 (2018).
21. C. Pang, Z. Hua, D. Zhou, H. Zhang, L. Chen, X. Bao, and Y. Dong, "Opto-mechanical time-domain analysis based on coherent forward stimulated Brillouin scattering probing," Optica **7**, 176–184 (2020).
22. H. Shin, J. A. Cox, R. Jarecki, A. Starbuck, Z. Wang, and P. T. Rakich, "Control of coherent information via on-chip photonic–phononic emitter–receivers," Nat. Commun. **6**, 6427 (2015).
23. E. A. Kittlaus, H. Shin, and P. T. Rakich, "Large Brillouin amplification in silicon," Nat. Photonics **10**, 463–467 (2016).
24. N. T. Otterstrom, R. O. Behunin, E. A. Kittlaus, Z. Wang, and P. T. Rakich, "A silicon Brillouin laser," Science **360**, 1113–1116 (2018).
25. M. Pang, X. Jiang, W. He, G. Wong, G. Onishchukov, N. Joly, G. Ahmed, C. Menyuk, and P. St.J. Russell, "Stable subpicosecond soliton fiber laser passively mode-locked by gigahertz acoustic resonance in photonic crystal fiber core," Optica **2**, 339–342 (2015).
26. W. E. née Zhong, B. Stiller, D. Elser, B. Heim, C. Marquardt, and G. Leuchs, "Depolarized guided acoustic wave Brillouin scattering in hollow-core photonic crystal fibers," Opt. Express **23**, 27707–27714 (2015).
27. W. Renninger, H. Shin, R. Behunin, P. Kharel, E. Kittlaus, and P. Rakich, "Forward Brillouin scattering in hollow-core photonic bandgap fibers," New J. Phys. **18**, 025008 (2016).
28. W. H. Renninger, R. O. Behunin, and P. T. Rakich, "Guided-wave Brillouin scattering in air," Optica **3**, 1316–1319 (2016).
29. J. R. Koehler, F. Köttig, B. M. Trabold, F. Tani, and P. St.J. Russell, "Long-lived refractive-index changes induced by femtosecond ionization in gas-filled single-ring photonic-crystal fibers," Phys. Rev. Appl. **10**, 064020 (2018).
30. F. Yang, F. Gyger, and L. Thévenaz, "Intense Brillouin amplification in gas using hollow-core waveguides," Nat. Photonics **14**, 700–708 (2020).
31. A. Iyer, W. Xu, J. E. Antonio-Lopez, R. A. Correa, and W. H. Renninger, "Ultra-low Brillouin scattering in anti-resonant hollow-core fibers," APL Photon. **5**, 096109 (2020).
32. P. Zhao, Y. Zhao, H. Bao, H. L. Ho, W. Jin, S. Fan, S. Gao, Y. Wang, and P. Wang, "Mode-phase-difference photothermal spectroscopy for gas detection with an anti-resonant hollow-core optical fiber," Nat. Commun. **11**, 847 (2020).
33. S. E. Bialkowski, *Photothermal Spectroscopy Methods for Chemical Analysis* (Wiley, 1996), Vol. **177**.
34. J. Han, K. Freel, and M. C. Heaven, "Rotational and vibrational energy transfer in vibrationally excited acetylene at energies near 6560cm^{-1}," J. Chem. Phys. **135**, 244304 (2011).
35. M. I. Hasan, N. Akhmediev, and W. Chang, "Empirical formulae for dispersion and effective mode area in hollow-core antiresonant fibers," J. Lightwave Technol. **36**, 4060–4065 (2018).
36. R. W. Boyd, *Nonlinear Optics* (Academic, 2020).
37. S. G. Johnson, M. Ibanescu, M. Skorobogatiy, O. Weisberg, J. Joannopoulos, and Y. Fink, "Perturbation theory for Maxwell's equations with shifting material boundaries," Phys. Rev. E **65**, 066611 (2002).
38. M. L. Povinelli, M. Lončar, M. Ibanescu, E. J. Smythe, S. G. Johnson, F. Capasso, and J. D. Joannopoulos, "Evanescent-wave bonding between optical waveguides," Opt. Lett. **30**, 3042–3044 (2005).
39. M. Li, W. Pernice, C. Xiong, T. Baehr-Jones, M. Hochberg, and H. Tang, "Harnessing optical forces in integrated photonic circuits," Nature **456**, 480–484 (2008).
40. A. Butsch, J. Koehler, R. Noskov, and P. St.J. Russell, "CW-pumped single-pass frequency comb generation by resonant optomechanical nonlinearity in dual-nanoweb fiber," Optica **1**, 158–164 (2014).
41. Y. Pan, D. Wang, Y. Wang, J. Liu, S. Wu, T. Qu, K. Yang, and H. Luo, "Monolithic cylindrical fused silica resonators with high Q factors," Sensors **16**, 1185 (2016).
42. W. Jin, H. Ho, Y. Cao, J. Ju, and L. Qi, "Gas detection with micro- and nano-engineered optical fibers," Opt. Fiber Technol. **19**, 741–759 (2013).
43. W. Jin, Y. Cao, F. Yang, and H. L. Ho, "Ultra-sensitive all-fibre photothermal spectroscopy with large dynamic range," Nat. Commun. **6**, 6767 (2015).
44. M. H. Frosz, R. Pennetta, M. T. Enders, G. Ahmed, and P. St.J. Russell, "Non-invasive real-time characterization of hollow-core photonic crystal fibers using whispering gallery mode spectroscopy," Opt. Express **27**, 30842–30851 (2019).
45. J. Jackle and K. Kawasaki, "Intrinsic roughness of glass surfaces," J. Phys. Condens. Matter **7**, 4351 (1995).
46. P. Roberts, F. Couny, H. Sabert, B. Mangan, D. Williams, L. Farr, M. Mason, A. Tomlinson, T. Birks, J. Knight, and P. St.J. Russell, "Ultimate low loss of hollow-core photonic crystal fibres," Opt. Express **13**, 236–244 (2005).
47. K. Han, J. Kim, and G. Bahl, "High-throughput sensing of freely flowing particles with optomechanofluidics," Optica **3**, 585–591 (2016).